Journal of Colloid and Interface Science 646 (2023) 703–710

Contents lists available at ScienceDirect

Journal of Colloid And Interface Science

journal homepage: www.elsevier.com/locate/jcis

Interphase stabilized electrospun SnO_2 fibers as alloy anode *via* restricted cycling for Li-ion capacitors with high energy and wide temperature operation

Manohar Akshay [a], Sundaramurthy Jayaraman [b], Mani Ulaganathan [c], Yun-Sung Lee [d,*], Vanchiappan Aravindan [a,*]

[a] Department of Chemistry, Indian Institute of Science Education and Research (IISER) Tirupati 517507, India
[b] Environmental & Water Technology Centre of Innovation, Ngee Ann Polytechnic, 535 Clementi Rd, 599489, Singapore
[c] Department of Sciences, Amrita School of Physical Sciences, Amrita Vishwa Vidyapeetham Coimbatore, 641112, India
[d] School of Chemical Engineering, Chonnam National University, Gwang-ju, 61186, Republic of Korea

GRAPHICAL ABSTRACT

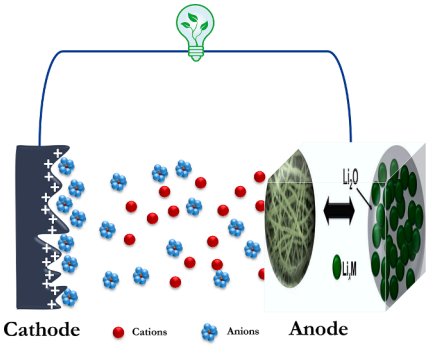

ARTICLE INFO

Keywords:
Li-ion capacitors
Alloy anode
SnO_2 nanofibers
stable SEI layer
In-situ impedance

ABSTRACT

The second-generation supercapacitor comprises the hybridized energy storage mechanism of Lithium-ion batteries and electrical double-layer capacitors, *i.e*, Lithium-ion capacitors (LICs). The electrospun SnO_2 nanofibers are synthesized by a simple electrospinning technique and are directly used as anode material for LICs with activated carbon (AC) as a cathode. However, before the assembly, the battery-type electrode SnO_2 is electrochemically pre-lithiated ($Li_xSn + Li_2O$), and AC loading is balanced with respect to its half-cell performance. First, the SnO_2 is tested in the half-cell assembly with a limited potential window of 0.005 to 1 V *vs*. Li to avoid the conversion reaction of Sn^0 to SnO_x. Also, the limited potential window allows only the reversible alloy/de-alloying process. Finally, the assembled LIC, AC/($Li_xSn + Li_2O$), displayed a maximum energy density of 185.88 Wh kg^{-1} with ultra-long cyclic durability of over 20,000 cycles. Further, the LIC is also exposed to various temperature conditions (–10, 0, 25, & 50 °C) to study the feasibility of using them in different environmental conditions.

* Corresponding authors.
E-mail addresses: leeys@chonnam.ac.kr (Y.-S. Lee), aravindan@iisertirupati.ac.in (V. Aravindan).

https://doi.org/10.1016/j.jcis.2023.05.091
Received 29 March 2023; Received in revised form 11 May 2023; Accepted 14 May 2023
Available online 19 May 2023

1. Introduction

With the rise in population, the demand for energy around the world is increasing aggressively. So, energy storage has become inevitable to meet the need of the growing population and the future generation. Hence, we have different energy storage methods such as mechanical, electrical, thermal, etc.; among them, electrochemical energy storage (mainly Batteries and Supercapacitors (Li, Na & K) [1–4] is one of the promising ones. Lithium-ion batteries (LIBs) are one of the most explored electrochemical energy storage devices as they have a high energy density, low self-discharge, environmental benignity, etc. [5–10]. However, it lacks the power density required for high-end applications such as electric and hybrid vehicles. On the other hand, supercapacitors are devices with high power density but lack energy density [11]. So, a goal arises for achieving a device with energy and power density to bridge the gap between LIBs and supercapacitors. Hence, an advanced form of the energy storage device, Lithium-ion capacitors (LICs), is proposed, which simultaneously have energy and power density in a single device. The LIC consists of a battery-type (faradaic process) electrode (especially anode) hybridized with the capacitive type (non-faradaic process) cathode. The new LIC is anticipated to deliver a higher energy density than the supercapacitors and a higher power density than LIBs. Furthermore, the LIC is as safe as an electrical double-layer capacitor (EDLC) as it will not cause thermal runaway compared with LIBs. Hence, LICs have a wide variety of applications, including spacecraft, power electronics, grid connections, railways, regenerative braking systems, etc. [12–15].

The overall power capability, energy density, and reaction rates of LIC depend upon the performance of the battery-type electrode. So, researchers are more focused on the development of the anodic part of the LICs, irrespective of Li-storage mechanisms [16–18]. Early researchers mostly attempted the utilization of various insertion-type anodes [19,20], but their energy density is inadequate for high-end applications. Nevertheless, graphitic carbon and $Li_4Ti_5O_{12}$-based LICs reached the commercial market, in which the former configuration requires an additional pre-lithiation step besides mass-balancing. Still, the capacity of the graphite is limited to 372 mAh g^{-1}. Hence, present-day research is transitioning from insertion-type to alloying/conversion mechanism with a reversible capacity of $>$ 500 mAh g^{-1} [21–28] for high-energy applications. In other words, moving from a single electron to a multi-electron reaction. Few reports are available on the utilization of conversion and alloying type anode for the fabrication of LICs, which we have summarized in our review [21]. Among the different alloying materials, SnO_2 is one of the promising candidates with high theoretical capacity (~782 mAh g^{-1}), low operating potential (less than 0.3 V *vs.* Li), high abundance, etc. However, the SnO_2 suffers from high volume variation (>200%) during cycling, resulting in pulverization of electrodes followed by capacity fading [7,29–32]. Various efforts are reported to mitigate these issues through morphological modification and synthesizing nanoparticles at various dimensions [33–38]. In the present work, we have synthesized pearl-string-like SnO_2 nanofibers through the electrospinning technique and used them as anodes for LIC. Prior to the fabrication of LIC, the mass-loading between the electrodes is adjusted based on the half-cell performance. Also, the battery-type electrode, SnO_2, is electrochemically pre-lithiated ($Li_xSn + Li_2O$). In both half-cell and full-cell assemblies, the electrospun SnO_2 fibers enhanced electrochemical activity. The feasibility of using such configurations in various environmental conditions is explored and discussed in detail.

2. Experimental section

2.1. Synthesis of SnO_2 nanofibers

One-dimensional electrospun SnO_2 nanofibers were synthesized by a simple electrospinning technique. In the typical procedure, 3 g of tin(II) chloride ($SnCl_2$) was added to 20 ml of dimethylformamide (DMF) and stirred for 1 h. Similarly, 4 g of polyvinylpyrrolidone (PVP, MW: 1,30,000) was added to 20 ml of ethanol and mixed for 1 h. Both solutions were finally mixed and stirred to obtain a homogenous solution. Finally, the mixed solution was loaded into a plastic syringe with an internal diameter of a pinhead of around 0.859 mm. Later, the pinhead was connected to a high-voltage supply that could generate a direct current voltage of up to 30 kV (ELECTROSPUNRA). The aluminium foil was used as the static collector. The distance between the needle and static collector was maintained at 16 cm with an applied ac voltage of 25 kV and a flow rate of 0.4 ml h^{-1}. The humidity level of the synthesis electrospinning chamber was maintained at about 35% for the whole experimental process. Finally, the synthesized fibers were collected and immediately preheated at 120 °C. The fibers were then further sintered at 600 °C, with a heating rate of 5 °C min^{-1} to 4 h under an air atmosphere to yield pearl-string-like SnO_2 nanofibers.

2.2. Material characterization

The purity and phase identification of the synthesized SnO_2 nanofiber was analyzed using powder X-ray diffraction (XRD) measurement (Rigaku D/teX Ultra 250 diffractometer; 40 kV, 200 mA, $\lambda = 1.5406$ Å with Cu Kα radiation). Raman spectroscopy analysis was performed using Lab Ram HR800 UV Raman microscope (Horiba Jobin-Yvon, France). The surface morphology and internal structure of the SnO_2 nanofibers were examined by a Field-emission scanning electron microscope (FE-SEM S-4700, Hitachi, Japan) and a High-resolution transmission electron microscope (HR-TEM, TECNAI, Philips, the Netherlands, 200 keV), respectively. Elemental composition and the surface electronic states of the nanofiber were investigated using X-ray photoelectron spectroscopy (XPS, Multilab 2000, UK; monochromatic Al Kα radiation $h\nu = 1486.6$ eV), High angle annular dark-field imaging (HAADF) detector and Energy-dispersive X-ray spectroscopy (EDS).

2.3. Electrochemical performance analysis

The SnO_2 nanofiber was tested as the negative electrode in the half-cell configuration with Li-metal foil as the counter/reference electrode. A simple hand-made technique was used to fabricate the electrodes. The SnO_2 nanofiber, conductive carbon (acetylene black), and binder (teflonized acetylene black – TAB-2) were mixed in the ratio of 2:2:1.5 in a mortar pestle using ethanol as the solvent. Initially, the SnO_2 nanofiber was weighed to the mortar pestle, and the conductive carbon was added. It was mixed thoroughly to have a uniform distribution of the acetylene black over the nanofiber. And then, the binder was weighed to it, followed by adding drops of ethanol solvent. This was mixed entirely, and a uniform circular thin layer of the free-standing electrode was made from it. The obtained thin layer of electrode material was punched over a 14 mm stainless-steel mesh current collector (Goodfellow, UK). Concurrently the activated carbon (AC, YP 80F Kuraray, Japan; Surface area: 2100 $m^2 g^{-1}$, Pore volume: 0.97 ml g^{-1}) electrode was also fabricated by the aforesaid hand-made method by mixing the AC, conductive carbon, and binder in 8:1:1 ratio in the mortar pestle using the same ethanol solvent. The thin AC electrode layer was punched over a 14 mm stainless-steel mesh. Both these electrodes are dried in the vacuum oven at 75 °C for more than 4 h before the cell fabrication.

The Li/SnO_2 and Li/AC half-cells were fabricated using 2016-type coin-cells inside an Argon-filled glove box (MBraun, Germany) with O_2 and H_2O levels less than 0.1 ppm. The Li/SnO_2 half-cell was fabricated so that the SnO_2 electrode was initially placed over the cathode cap, and then the Whatman paper (1825–047, GF/F) separator was kept covering it. It was wetted by the electrolyte (1 M $LiPF_6$ dissolved in ethylene carbonate (EC) and dimethyl carbonate (DMC) in a 1:1 ratio, Tomiyama, Japan). The Li-metal foil was placed over the separator, and finally, it was crimped after closing it with an anode cap. Similarly, the Li/AC half-cell was also fabricated, and both were kept for electrochemical testing after a 6 h rest period. The Li/SnO_2 and Li/AC cells

were kept for galvanostatic charge–discharge in the potential range of 0.005 to 1 V *vs.* Li and 1.5 to 4.5 V *vs.* Li, respectively. Also, cyclic voltammetry studies were performed for the Li/SnO_2 half-cell at a scan rate of 0.1 mV s^{-1}.

The AC/(Li_xSn + Li_2O)-based LIC was fabricated by combining the pre-lithiated SnO_2 electrode with the AC electrode under balanced loading conditions. In a typical electrochemical pre-lithiation process, Li/SnO_2 half-cell was kept for two complete charge–discharge cycles. After the third discharge, the cell was de-crimped inside the glove box, and the pre-lithiated SnO_2 electrode was separated. This electrode was then paired with the mass-balanced AC electrode to form LIC, AC/(Li_xSn + Li_2O). After 8 h of the rest period, the LIC was subjected to GCD analysis from a 1.2 to 4.2 V potential window using a Biologic BCS 805 (France) battery tester. An *in-situ* impedance spectroscopy analysis was performed to examine the interfacial properties, and the performance of LIC in different climatic conditions was also analyzed using an environmental chamber (Espec, Japan).

3. Results and discussion

The crystalline structure and phase purity of SnO_2 nanofibers is examined using the powder X-ray diffraction (XRD) measurements (Fig. 1 (a)). The diffraction peaks correspond to the Cassiterite phase with lattice parameters $a = b = 4.737$ Å and $c = 3.185$ Å and 136: *P*42/*mnm* space group (DB Card Number: 04–003-0649, JCPDS number: 41–1445). The comparison of XRD with the standard data and with post-long-term cycling is given in figure S1. The crystallite size of SnO_2 nanofiber is calculated using Scherrer's equation ($D = 0.9\lambda/\beta \cos\theta$) and found to be 18.42 nm. The surface of the SnO_2 is studied from the nitrogen sorption studies (figure S2). It has a BET surface area and pore volume of 41.495 m^2 g^{-1} and 0.110 cc g^{-1}, respectively. The pore diameter is observed to be around ~ 6.08 nm which is clearly in the mesoporous region. Fig. 1 (b-c) shows the field emission-scanning electron microscopic (FE-SEM) images of as-spun fibers, which show a very smooth surface morphology with a fiber diameter of 100 to 200 nm. After the calcination process at 600 °C shows the presence of interconnected particulate morphology with long-chain. The appearance of such particulate morphology is similar to the pearl strings. The transition from smooth to particulate morphology is mainly due to the decomposition of the polymer backbone. The pearl-string-like morphology is evident from the FESEM pictures with different magnifications (Fig. 1(d-f)). Further analysis of the morphology, size, and internal structure of the SnO_2 nanofiber was performed using a high-resolution transmission electron microscope (HR-TEM), and the results are given in Fig. 1(g, h). The TEM images can further confirm the pearl-string structure observed from the spherical-shaped pearls connected by a long string (Fig. 1(d)). It is obvious to note that every spherical-shaped particulate is found to be single-crystalline in nature. The *d* spacing of lattice fringes was calculated and found to be 2.63 Å. The concentric bright spots on the selected area electron diffraction (SAED) further confirm the crystalline nature of the SnO_2 nanofibers (Fig. 1(i)).

X-ray photoelectron spectroscopy (XPS) analysis was performed in order to examine the surface chemical compositions and the redox states of SnO_2 nanofiber (Fig. 2(a, b)). The deconvoluted Sn 3d spectra (Fig. 2 (a)) show peaks at 486.8 and 495.25 eV corresponding to Sn $3d_{5/2}$ and Sn $3d_{3/2}$, respectively, which infer the existence of Sn in the 4 + state

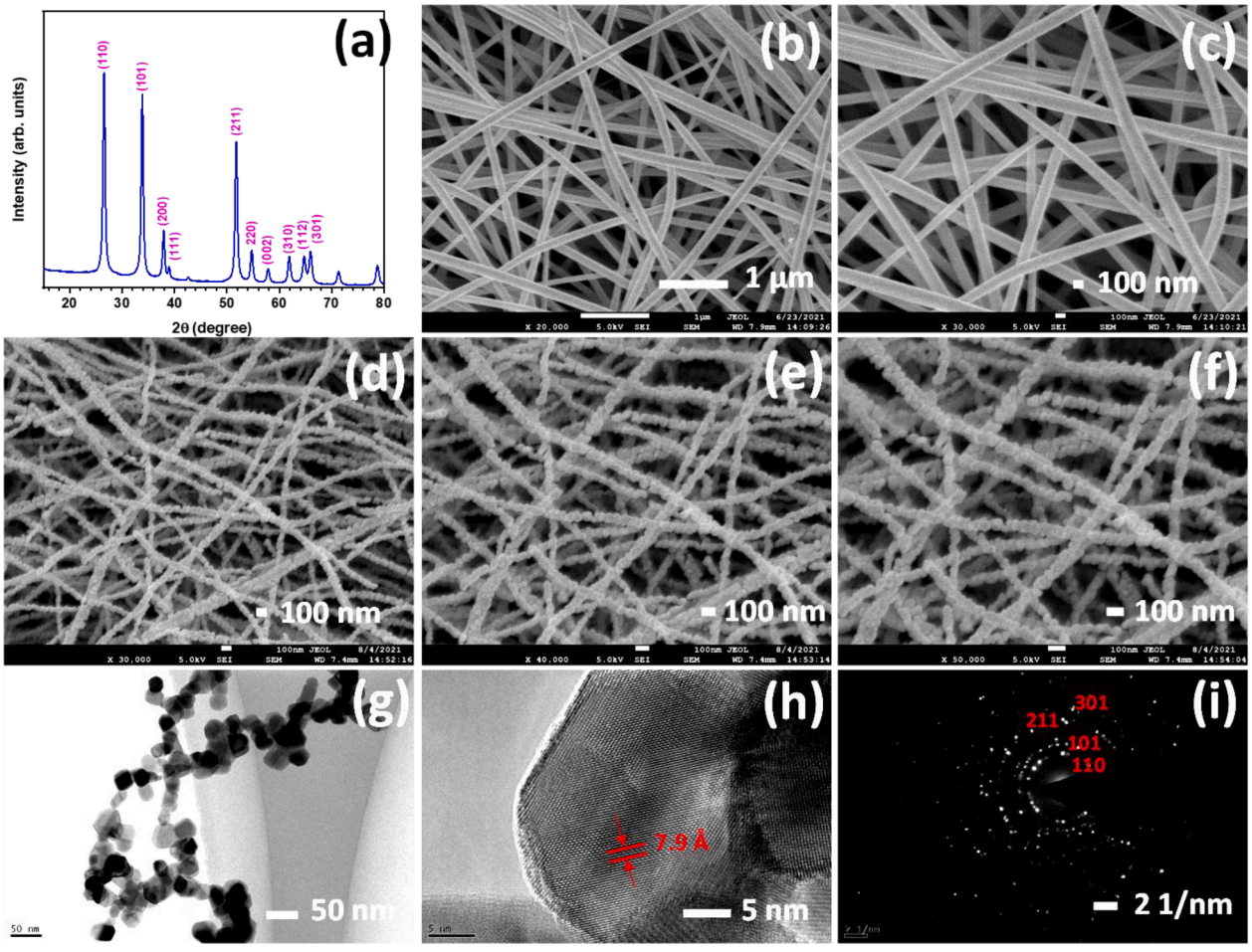

Fig. 1. Physical characterization of SnO_2 nanofiber: (a) Powder-XRD pattern, (b-c) FE-SEM images of as-spun SnO_2 fibers at different magnifications, (d-f) FESEM images of calcined SnO_2 fibers at different magnifications, (g, h) HR-TEM images, and (i) SAED pattern.

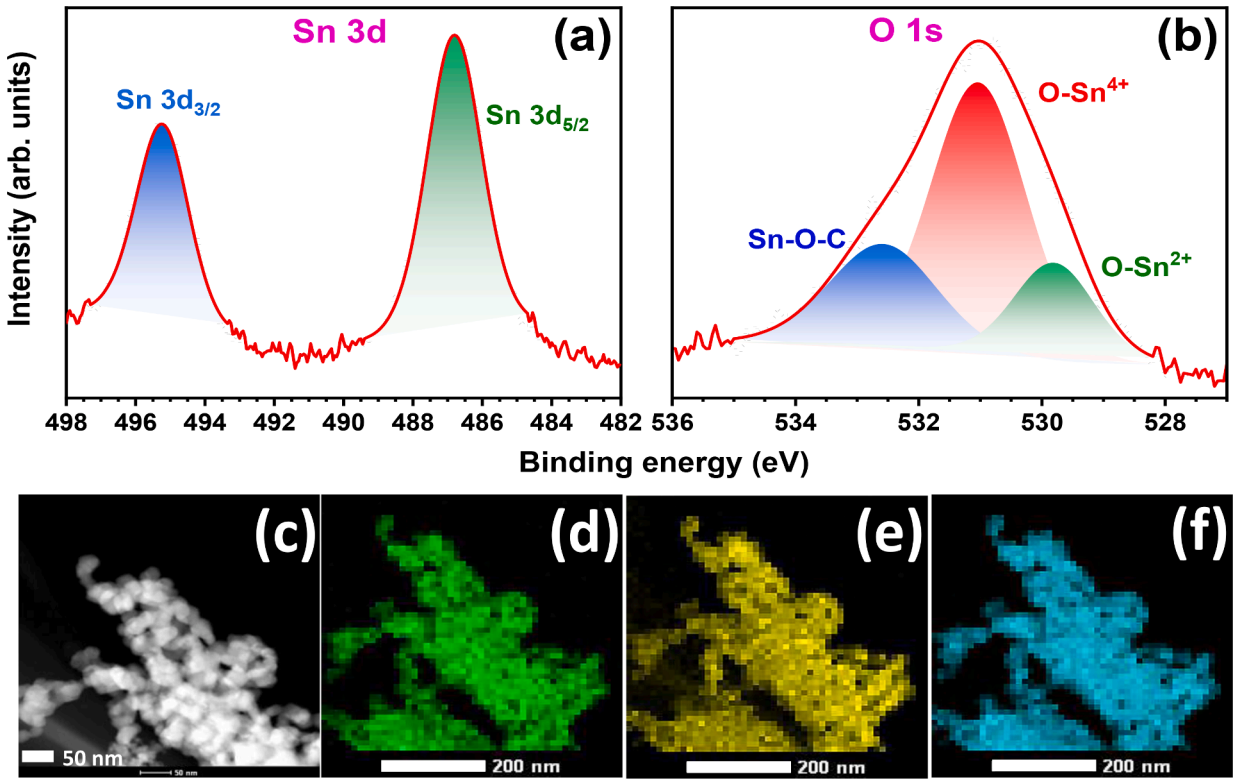

Fig. 2. (a, b) Deconvoluted XPS spectra of SnO_2 nanofibers, (c) HAADF-STEM image, and (d-f) EDS mappings of SnO_2 nanofiber.

[39]. Moreover, the ~ 8 eV binding energy difference between Sn $3d_{5/2}$ and Sn $3d_{3/2}$ corresponds to the binding energy of Sn's 3d electron, which also agrees with the standard database [33,40]. The O 1s spectrum (Fig. 2(b)) is deconvoluted into three asymmetric peaks observed at 529.8, 531.05, and 532.6 eV [40]. The STEM image and EDS mapping are given in Fig. 2(c) and Fig. 2(d-f), respectively. The elemental distribution displayed in the EDS mapping images illustrates the existence and homogeneous distribution of Sn and O.

3.1. Electrochemical performance

Cyclic voltammetry (CV) analysis was carried out for the SnO_2 nanofiber from the potential range of 0.005 to 1 V *vs.* Li at 0.1 mV s^{-1} scan rate. The CV profiles are given in Fig. 3(a) (first 10 cycles) and have three cathodic peaks and an anodic peak observed in the first cycle. The cathodic peak observed at ~ 0.77 and ~ 0.63 V *vs.* Li corresponds to the reduction of SnO_2 to Sn and Li_2O and solid electrolyte interphase (SEI) layers formation. The other cathodic peak at ~ 0.12 V *vs.* Li indicates the alloy formation of Sn with the Li-ions (Li_xSn) [30,36,41]. The anodic peak observed at ~ 0.56 V *vs.* Li is associated with the formation of metallic Sn (Sn^0) from the Li_xSn alloy (figure S1). From the second cycle onwards, the cathodic peaks at ~ 0.77 and ~ 0.63 V *vs.* Li in the first cycle are absent, which is common for Sn-based anodes and indicates the stable performance of the SnO_2 anode within the restricted potential operation. The galvanostatic charge–discharge (GCD) analysis was performed for the SnO_2 nanofiber from 0.005 to 1 V *vs.* Li at a current density of 80 mA g^{-1}, as shown in Fig. 3(b). The Li/SnO_2 half-cell delivered an initial discharge capacity of 2251 mAh g^{-1} with a coulombic efficiency of 31.19%. The initial coulombic efficiency is less due to the degradation of the electrolyte and subsequent formation of the SEI layer, which also causes an irreversible consumption of the Li-ions. As a result, a huge irreversibility capacity is observed in the first cycle. The GCD was performed for over 50 cycles with ~ 74% retention and is given in Fig. 3(c). Moreover, the Li/SnO_2 cell is also subjected to charge–discharge at different current rates from 0.05 to 1.5 A g^{-1} (Fig. 3 (d, e)). The half-cell exhibited a better rate performance at different current rates. As the current rate increases, we see a specific capacity decrease. However, over > 93% of the initial capacity is regained when the current rate is again decreased, which shows the reversibility and stability of the SnO_2 nanofibers.

It is well-known inferior SEI formation is one of the prime issues of both conversion and alloy anodes. The robust and stable SEI formation certainly leads to enhanced electrochemical performance. In this line, in order to probe such stable electrochemical performance, we have performed the *in-situ*-electrochemical impedance spectroscopy (*in-situ*-EIS) and illustrated in Fig. 4. The *in-situ*-EIS analysis was recorded for the 1^{st}, 5^{th}, 10^{th}, 50^{th}, and 100^{th} cycles (figure S3). It is observed that after the initial discharge, there is an increase in the transfer resistance (R_{CT}), primarily due to the irreversible capacity loss due to the SEI layer formation. However, after the first discharge, the R_{CT} became constant and persisted till the end of the 100th cycle, which accounts for the robust SEI layer formation in Li/SnO_2, which is the primary reason for the excellent electrochemical activity of SnO_2 in half-cell assembly. This performance logically led us to the exploration of a battery-type electrode in full-cell assembly with an AC electrode. The Nyquist plot and the electrical equivalent circuit are also given in the supplementary part (figure S4), which shows that the R_{CT} value before and after cycling is around 121 and 229.4 Ω, respectively.

The Li/AC half-cell is fabricated and tested in the potential window of 1.5 to 4.5 V *vs.* Li. The charge is stored in Li/AC half-cell by a simple capacitive type adsorption/desorption mechanism, *i.e.*, physisorption. During charging/discharging, the Li^+ and PF_6^- ions are adsorbed/desorbed; hence, energy storage/energy delivery happens. The Li/AC has an initial discharge capacity of 152 mAh g^{-1} and maintains ~ 142 mAh g^{-1} as a specific capacity even after 200 cycles (figure S5). Generally, the LIC consists of a battery-type anode and a capacitor-type cathode hybridized together. In the anode, the faradaic reaction occurs (here, alloying reaction); in the cathode, simple non-faradaic adsorption/desorption occurs. Since both electrodes have different energy storage mechanisms, there is a kinetic imbalance between the two. Hence, mass

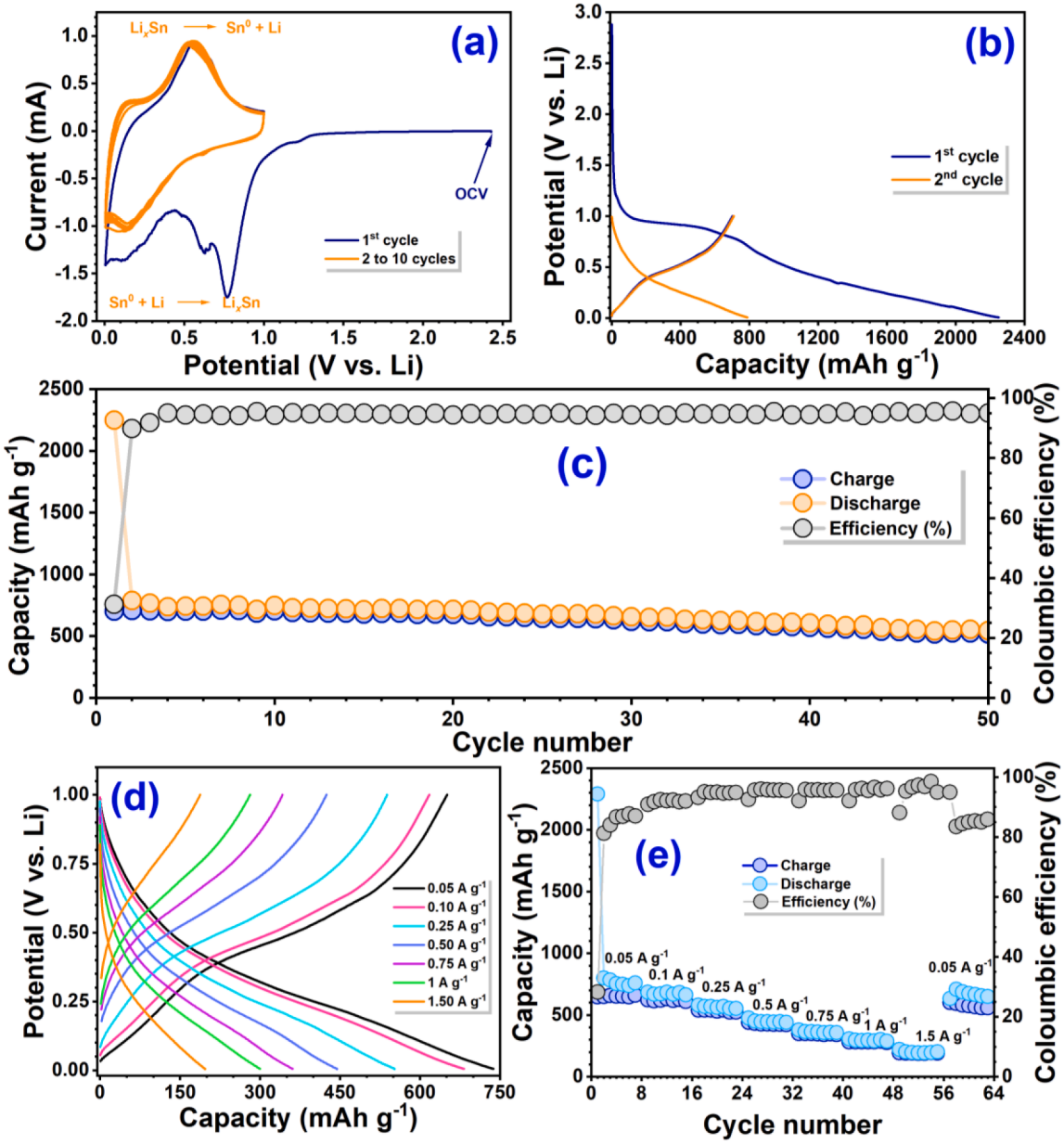

Fig. 3. Electrochemical performance of Li/SnO_2 half-cells (a) Cyclic voltammogram recorded at a scan rate of 0.1 mV s^{-1}, (b) charge–discharge profile (first two cycles) at a current density of 0.08 A g^{-1}, (c) galvanostatic charge–discharge profile with coloumbic efficiency, (d) charge–discharge profile at different current rates (0.05 to 1.5 A g^{-1}), and (e) rate capability studies.

balancing is desperately required between the two electrodes to realize high energy density. The mass is balanced based on the half-cell performance of both electrodes (*vs.* Li) by using the following equation,

$$M_1C_1 = M_2C_2$$

Where M_1 is the mass of SnO_2, C_1 is the specific capacity of SnO_2, M_2 is the mass of AC, and C_2 is the specific capacity of AC.

The AC/SnO_2 LIC is fabricated such that, initially, the battery-type electrode SnO_2 is pre-lithiated ($Li_xSn + Li_2O$), followed by pairing it with the AC electrode. In a typical process, the Li/SnO_2 half-cell is fabricated and kept for GCD for a couple of cycles. After two cycles, the cell is discharged to yield the $Li_xSn + Li_2O$ phase. The pre-lithiated SnO_2 half-cell is dismantled and paired with the mass-balanced AC electrode. The electrochemical performance of AC/($Li_xSn + Li_2O$) full-cell assembly at different temperatures is given in Fig. 5. Fig. 5(a-e) depicts the E_{cell} *vs.* time graph of LIC at different current rates and temperatures ranging from –10 to 50 °C. In a typical charge–discharge process, the alloying/de-alloying reaction with Li happens *via* the fardaic process, whereas to maintain the charge- neutrality in the cell, the non-faradaic process occurs on the counter electrode. Unlike cations only involved in the faradaic process, both anions (PF_6^-) and cations (Li^+) involve in the non-faradaic process due to the wider operating potential of the cell [42]. Apparently, in all the cases, an increase in the current rate tends to decrease the charge-storage time, which is quite common for all types of a cell due to the insufficient time for the faradaic process or surface only involved in the reaction instead of bulk. Here, the applied current density, energy density, and power density values are calculated based on the total active mass loading in both the anode and cathode.

The Ragone plot given in Fig. 5(f) compares the energy density and power density of LIC at different current rates and temperatures. The plot shows that the LIC exhibits its best performance at room temperature. The AC/SnO_2 LIC, with anodic and cathodic mass 1 and 4.8 mg, respectively, delivers a maximum energy density of 185.88 Wh kg^{-1} and power density of 7.7 kW kg^{-1} at room temperature. The observed values

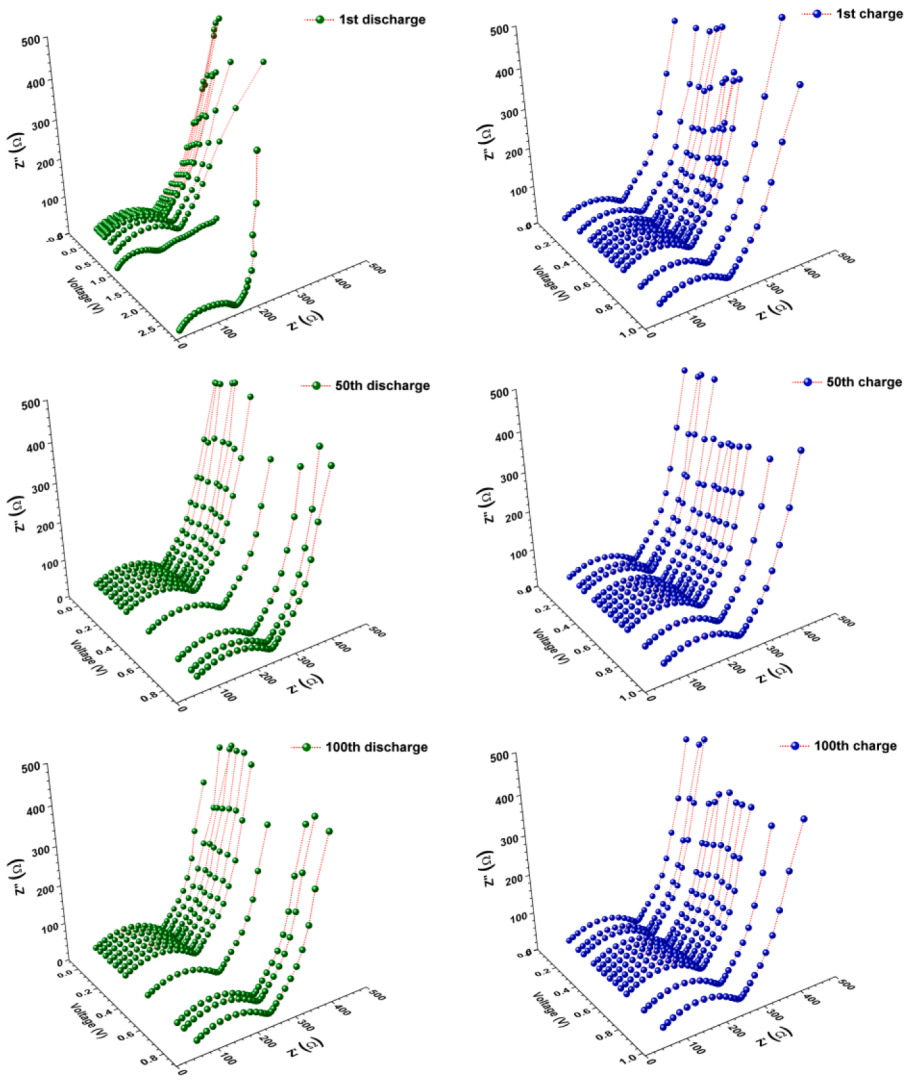

Fig. 4. *in-situ*-electrochemical impedance spectroscopy (*in-situ*-EIS) profile of Li/SnO_2 half-cell. a.c. impedance profile of 1st, 50th' and 100th charge–discharge at different potentials.

are consistent with the reported values on the conversion and alloy-anode-based LICs [43-45]. We have also investigated the possibility of the AC/SnO_2 LIC under different environmental conditions. The rate performance is examined at different temperatures (–10, 0, 10, 25 & 50 °C) and obtained that, in addition to the room temperature, the LIC exhibits better performance at higher temperatures as well. This clearly indicates the possibility of using various environmental conditions. Interestingly, a very decent energy density of 143.31 Wh kg^{-1} is registered at 50 °C. As expected, a notable decline in the Li-storage performance is observed at low-temperature conditions (–10, 0, & 10 °C), which is mainly associated with the freezing of the liquid electrolyte. The GCD cycling studies were also performed for AC/(Li_xSn + Li_2O)-based LIC at different temperatures, and the capacity is normalized to 100% for easier comparison, as shown in Fig. 5(g). Though the LIC rendered slightly inferior performance at sub-zero temperature conditions (–10 °C), but displayed an excellent cycling profile at high temperatures (50 ^{0}C) primarily due to the increase in ionic conductivity when temperature increases [42]. Generally, at high temperatures (50 °C), the electrochemical activity of the liquid electrolyte-based LIC exhibit very worse performance originating from the inevitable side reaction with the electrode. But, in this case, due to the robust and stable SEI layer (validated through *in-situ* impedance) certainly escalates such side reactions and translates to better durability. Apparently, irrespective of the temperature conditions, the cell showed a remarkable performance, and we strongly believe that the stable interphase, *i.e.*, the robust SEI layer is the prime reason for such performance. We could also observe a dominating performance of our LIC when compared with the previously reported works with the alloy-type anode (Table S1). In addition, the long-term cycling was performed at a current density of 1.5 A g^{-1} (Fig. 5(h)) and displayed remarkable capacity retention of ~ 78 % even after 20,000 cycles which is close to the practical limitation of 80% retention. Overall, the LIC exhibited better performance, and further studies are in progress to improve the energy density at higher power rates. And, to understand the unique and robust SEI formed at the interphase is also underway.

4. Conclusion

We have successfully fabricated a LIC by utilizing pearl-string-like SnO_2 nanofibers as anode and commercial AC as the positive electrode. The SnO_2 nanofibers were synthesized from $SnCl_2$ precursors by a simple electrospinning technique. The nano-string structure enhanced the electrochemical properties, achieving better cyclic performance. The morphological modification of the SnO_2 contributed to the sturdy SEI layer, which in turn alleviated the pulverization of electrodes during cycling. The interfacial properties were initially analyzed using an *in-*

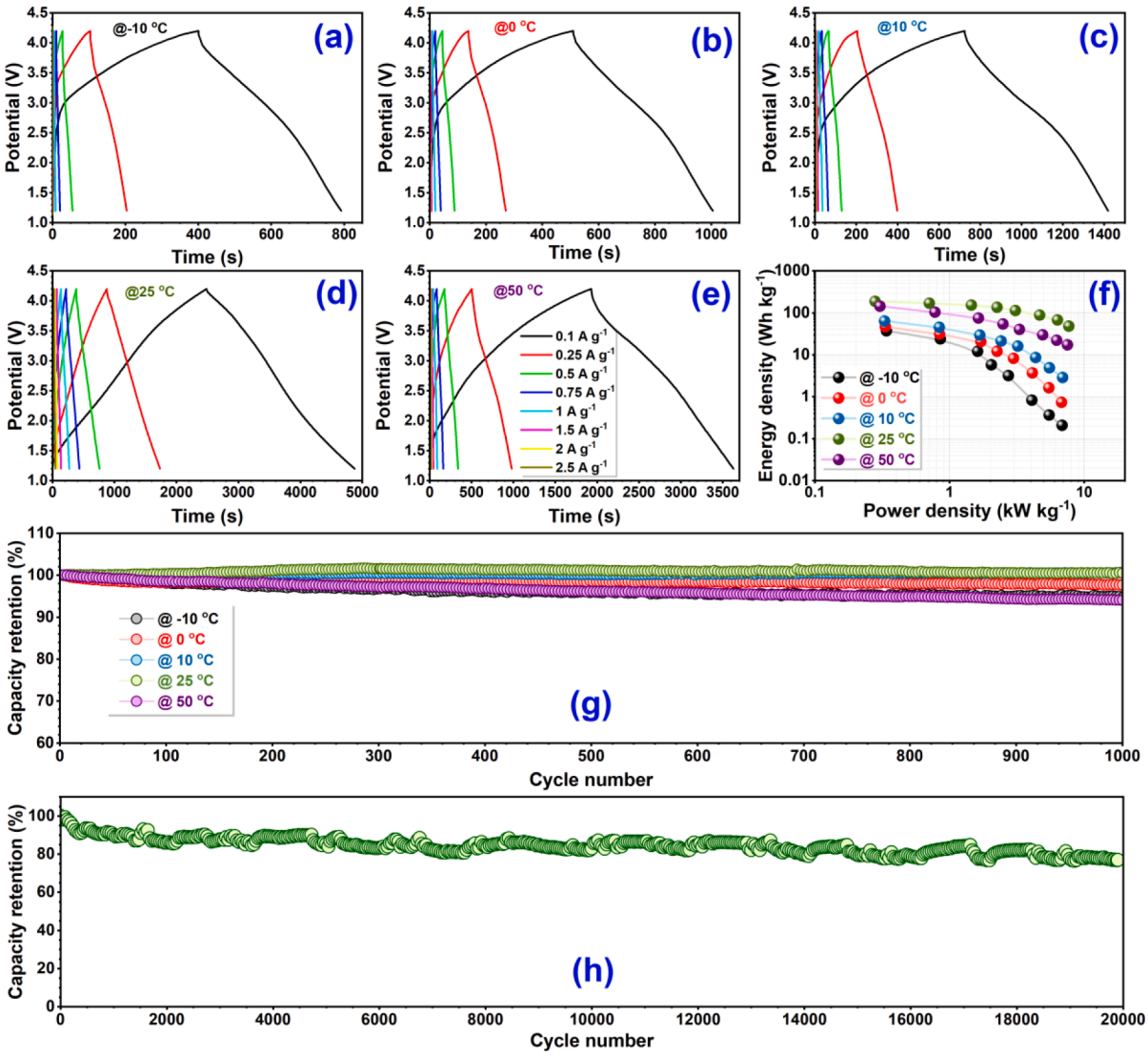

Fig. 5. Electrochemical performance of fabricated AC/(Li_xSn + Li_2O)-based LIC: (a-e) galvanostatic charge–discharge at different temperatures (–10, 0, 10, 25, and 50 °C), (f) Ragone plot comparing energy density and power density at different temperatures, (g) long-term cyclic performance at different temperatures at a current density of 0.75 A g^{-1}, and (h) long-term cycling stability at room temperature at a current density of 1.5 A g^{-1}.

situ-impedance study, and it confirms the robustness of the SEI formed over the alloy-type SnO_2. The AC/(Li_xSn + Li_2O)-based LIC delivered a maximum energy density of 185.88 Wh kg^{-1} at ambient temperature conditions. The pearl-string-like structure of SnO_2 primarily contributed AC/(Li_xSn + Li_2O) LIC to have remarkable capacity retention of ~ 78% even after 20,000 cycles. The performance of LIC in different environmental conditions was also evaluated with excellent durability, irrespective of the temperature conditions for 1000 cycles. Overall, the results obtained from our studies are momentous, and hence, the SnO_2 nanofibers have a promising potential to be employed in commercial cells.

CRediT authorship contribution statement

Manohar Akshay: Conceptualization, Investigation, Writing – original draft. **Sundaramurthy Jayaraman:** Methodology, Investigation, Resources. **Mani Ulaganathan:** Investigation, Resources. **Yun-Sung Lee:** Resources, Writing – original draft, Funding acquisition. **Vanchiappan Aravindan:** Conceptualization, Writing – review & editing, Supervision, Funding acquisition.

Declaration of Competing Interest

The authors declare that they have no known competing financial interests or personal relationships that could have appeared to influence the work reported in this paper.

Data availability

Data will be made available on request.

Acknowledgment

YSL acknowledges the financial support from the National Research Foundation of Korea (NRF) grant funded by the Korean government (Ministry of Science, ICT&Future Planning) (No. RS-2023-00208361). VA acknowledges financial support from the Science and Engineering Research Board, a statutory body of the Department of Science and Technology, Govt. of India, through the Nanomisson (DST/NM/TUE/EE-03/2019-1G-IISERTp) and Swarnajayanti Fellowship (SB/SJF/2020-21/12).

Data availability statement

Data will be made available on reasonable request to the corresponding author

Appendix A. Supplementary material

Supplementary data to this article can be found online at https://doi.org/10.1016/j.jcis.2023.05.091.

References

[1] J.-Z. Guo, et al., Heterogeneous NASICON-Type Composite as Low-cost, high-performance cathode for sodium-ion batteries, Adv. Funct. Mater. 32 (2022) 2209482.

[2] H. Liu, et al., High sulfur loading and shuttle inhibition of advanced sulfur cathode enabled by graphene network skin and N, P, F-doped mesoporous carbon interfaces for ultra-stable lithium sulfur battery, Nano Res. Energy 2 (2023) e9120049.

[3] X.-T. Wang, et al., An advanced cathode composite for co-utilization of cations and anions in lithium batteries, J. Mater. Sci. Technol. 102 (2022) 72–79.

[4] G. Liang, et al., Building durable aqueous K-ion capacitors based on MXene family, Nano Res. Energy 1 (2022) e9120002.

[5] V. Etacheri, R. Marom, R. Elazari, G. Salitra, D. Aurbach, Challenges in the development of advanced Li-ion batteries: a review, Energy Environ. Sci. 4 (2011) 3243–3262.

[6] J.-M. Tarascon, M. Armand, Issues and challenges facing rechargeable lithium batteries. in *Materials for Sustainable*, Energy (2010) 171–179, https://doi.org/10.1142/9789814317665_0024.

[7] X. Wang, et al., SnO_2/Sn/Carbon nanohybrid lithium-ion battery anode with high reversible capacity and excellent cyclic stability, Nano Sel. 2 (2021) 642–653.

[8] D.S. Baji, S.V. Nair, A.K. Rai, Highly porous disk-like shape of Co_3O_4 as an anode material for lithium ion batteries, J. Solid State Electrochem. 21 (2017) 2869–2875.

[9] K.Y. Yasoda, D.S. Baji, M.S. Kumar, D. Santhanagopalan, S.K. Batabyal, Sustainable development of manganese sulfoselenide nanoparticles anchored graphene oxide nanocomposite for high-performance supercapacitor and lithium-ion battery applications, J. Alloys Compd. 930 (2023), 167282.

[10] K. Mariyappan, T. Mahalakshmi, T.S. Roshni, P. Ragupathy, M. Ulaganathan, Nanocatalyzed PtNi Alloy Intact @3D Graphite Felt as an effective electrode for super power redox flow battery, Adv. Mater. Interfaces 10 (2023) 2202007.

[11] V. Prabu, K. Geetha, R. Sekar, M. Ulaganathan, Binder-free electro-deposited MnO_2@3D carbon felt network: a positive electrode for 2V aqueous supercapacitor, Energy Technol. 11 (2023) 2201345.

[12] J. Ding, W. Hu, E. Paek, D. Mitlin, Review of hybrid ion capacitors: from aqueous to lithium to sodium, Chem. Rev. 118 (2018) 6457–6498.

[13] A. González, E. Goikolea, J.A. Barrena, R. Mysyk, Review on supercapacitors: technologies and materials, Renew. Sustain. Energy Rev. 58 (2016) 1189–1206.

[14] J.J. Lamb, O.S. Burheim, Lithium-ion capacitors: a review of design and active materials, Energies 14 (2021) 1–27.

[15] Poonam, Sharma, K., Arora, A. & Tripathi, S. K. Review of supercapacitors: Materials and devices. *J. Energy Storage* **21**, 801–825 (2019).

[16] Y. Liu, et al., Metallurgical pyrolysis toward Co@Nitrogen-doped carbon composite for lithium storage, Green Energy Environ. 6 (2021) 91–101.

[17] W. Wang, et al., Defect engineering in molybdenum-based electrode materials for energy storage eScience 2 (2022,) 278–294.

[18] J.-H. Zhang, et al., Vanadium nitride nanoparticles embedded in carbon matrix with pseudocapacitive behavior for high performance lithium-ion capacitors, Rare Met. 41 (2022) 2460–2469.

[19] V. Aravindan, J. Gnanaraj, Y.-S. Lee, S. Madhavi, Insertion-type electrodes for nonaqueous Li-Ion capacitors, Chem. Rev. 114 (2014) 11619–11635.

[20] S. Natarajan, Y.-S. Lee, V. Aravindan, Biomass-derived carbon materials as prospective electrodes for high-energy lithium- and sodium-ion capacitors, Chem. – An Asian J. 14 (2019) 936–951.

[21] V. Aravindan, Y.-S. Lee, Building next-generation li-ion capacitors with high energy: an approach beyond intercalation, J. Phys. Chem. Lett. 9 (2018) 3946–3958.

[22] V. Aravindan, Y. Lee, S. Madhavi, Research progress on negative electrodes for practical Li-Ion batteries: beyond carbonaceous anodes, Adv. Energy Mater. 5 (2015).

[23] J.A. Lewis, K.A. Cavallaro, Y. Liu, M.T. McDowell, The promise of alloy anodes for solid-state batteries, Joule 6 (2022) 1418–1430.

[24] M. Akshay, R. Belgamwar, S. Praneetha, V. Polshettiwar, V. Aravindan, Defect engineered dendritic fibrous nanosilica as prospective alloy anode for the fabrication of high-energy li-ion capacitors with ultralong durability, ACS Mater. Lett. 5 (2023) 715–721.

[25] P. Sennu, S. Madhavi, V. Aravindan, Y.-S. Lee, Co_3O_4 nanosheets as battery-type electrode for high-energy Li-Ion Capacitors: a sustained li-storage via conversion pathway, ACS Nano 14 (2020) 10648–10654.

[26] M. Akshay, K. Subramanyan, M.L. Divya, Y.-S. Lee, V. Aravindan, Choice of Binder on Conversion Type CuO Nanoparticles toward Building High Energy Li-Ion Capacitors: An Approach Beyond Intercalation, Adv. Mater. Technol. 7 (2022) 2200423.

[27] K. Subramanyan, M. Akshay, Y.-S. Lee, V. Aravindan, Fabrication of Na-Ion Full-Cells using Carbon-Coated $Na_3V_2(PO_4)_2O_2F$ Cathode with Conversion Type CuO Nanoparticles from Spent Li-Ion Batteries, Small Methods 6 (2022) 2200257.

[28] S. Natarajan, M. Akshay, V. Aravindan, $MnCO_3$ Cuboids from Spent LIBs: A New Age Displacement Anode to Build High-Performance Li-Ion Capacitors, Small 19 (2023) 2206226.

[29] M. Akshay, S. Praneetha, Y.-S. Lee, V. Aravindan, Hierarchical SnO_2@PC@PANI composite via in-situ polymerization towards next-generation Li-ion capacitor by limiting alloying process with high energy, wide temperature performance, and cyclability, Electrochim. Acta 439 (2023), 141599.

[30] V. Aravindan, K.B. Jinesh, R.R. Prabhakar, V.S. Kale, S. Madhavi, Atomic layer deposited (ALD) SnO_2 anodes with exceptional cycleability for Li-ion batteries, Nano Energy 2 (2013) 720–725.

[31] Y. Wang, et al., Designed hybrid nanostructure with catalytic effect: beyond the theoretical capacity of SnO_2 anode material for lithium ion batteries, Sci. Rep. 5 (2015) 1–8.

[32] M.V. Reddy, G.V. Subba Rao, B.V.R. Chowdari, Metal oxides and oxysalts as anode materials for Li Ion batteries, Chem. Rev. 113 (2013) 5364–5457.

[33] M.L. Divya, S. Praneetha, Y.-S. Lee, V. Aravindan, Next-generation Li-ion capacitor with high energy and high power by limiting alloying-intercalation process using SnO_2@Graphite composite as battery type electrode, Compos. Part B Eng. 230 (2022), 109487.

[34] Z. Wen, Q. Wang, Q. Zhang, J. Li, In situ growth of mesoporous SnO_2 on multiwalled carbon nanotubes: a novel composite with porous-tube structure as anode for lithium batteries, Adv. Funct. Mater. 17 (2007) 2772–2778.

[35] Zhang, L., Wu, H. Bin, Liu, B. & (David) Lou, X. W. Formation of porous SnO_2 microboxes via selective leaching for highly reversible lithium storage. *Energy Environ. Sci.* **7**, 1013–1017 2014.

[36] V. Aravindan, et al., Does carbon coating really improves the electrochemical performance of electrospun SnO_2 anodes? Electrochim. Acta 121 (2014) 109–115.

[37] B.P. Vinayan, S. Ramaprabhu, Facile synthesis of SnO_2 nanoparticles dispersed nitrogen doped graphene anode material for ultrahigh capacity lithium ion battery applications, J. Mater. Chem. A 1 (2013) 3865–3871.

[38] P. Sennu, V. Aravindan, Y.-S. Lee, Marine algae inspired pre-treated SnO_2 nanorods bundle as negative electrode for Li-ion capacitor and battery: an approach beyond intercalation, Chem. Eng. J. 324 (2017) 26–34.

[39] J. Zhang, et al., Au nanoparticle-decorated porous SnO_2 hollow spheres: a new model for a chemical sensor, J. Mater. Chem. 20 (2010) 6453–6459.

[40] X. Han, et al., Sonochemistry-enabled uniform coupling of SnO_2 nanocrystals with graphene sheets as anode materials for lithium-ion batteries, RSC Adv. 9 (2019) 5942–5947.

[41] Y. Jiang, T. Yuan, W. Sun, M. Yan, Electrostatic spray deposition of porous SnO_2/Graphene anode films and their enhanced lithium-storage properties, ACS Appl. Mater. Interfaces 4 (2012) 6216–6220.

[42] M.L. Divya, S. Natarajan, Y.S. Lee, V. Aravindan, Achieving high-energy dual carbon Li-ion capacitors with unique low- And high-temperature performance from spent Li-ion batteries, J. Mater. Chem. A 8 (2020) 4950–4959.

[43] X. Liu, et al., Silicon/copper dome-patterned electrodes for high-performance hybrid supercapacitors, Sci. Rep. 3 (2013) 3183.

[44] R. Yi, et al., High-performance hybrid supercapacitor enabled by a high-rate Si-based anode, Adv. Funct. Mater. 24 (2014) 7433–7439.

[45] J. Luo, et al., Pillared structure design of MXene with ultralarge interlayer spacing for high-performance lithium-ion capacitors, ACS Nano 11 (2017) 2459–2469.